MATERIALS SCIENCE

One-step volumetric additive manufacturing of complex polymer structures

Maxim Shusteff,[1,2]* Allison E. M. Browar,[1,3] Brett E. Kelly,[1,4] Johannes Henriksson,[1,5] Todd H. Weisgraber,[1] Robert M. Panas,[1] Nicholas X. Fang,[6]* Christopher M. Spadaccini[1]*

Copyright © 2017 The Authors, some rights reserved; exclusive licensee American Association for the Advancement of Science. No claim to original U.S. Government Works. Distributed under a Creative Commons Attribution NonCommercial License 4.0 (CC BY-NC).

Two limitations of additive manufacturing methods that arise from layer-based fabrication are slow speed and geometric constraints (which include poor surface quality). Both limitations are overcome in the work reported here, introducing a new volumetric additive fabrication paradigm that produces photopolymer structures with complex nonperiodic three-dimensional geometries on a time scale of seconds. We implement this approach using holographic patterning of light fields, demonstrate the fabrication of a variety of structures, and study the properties of the light patterns and photosensitive resins required for this fabrication approach. The results indicate that low-absorbing resins containing ~0.1% photoinitiator, illuminated at modest powers (~10 to 100 mW), may be successfully used to build full structures in ~1 to 10 s.

INTRODUCTION

The paradigm of building from the bottom up, known as additive manufacturing (AM), is revolutionizing three-dimensional (3D) fabrication. The point-by-point and layer-by-layer techniques that characterize AM systems are advantageous owing to their generality, which allows broad geometric versatility. The AM approach therefore offers unprecedented customization and flexibility, where every part can be different from its predecessor. Moreover, complex structures that cannot be produced by traditional subtractive methods have become routinely possible by additive methods (*1*).

Along with these advantages, AM methods have also imposed their own new set of fabrication constraints. Two of the most significant are slow build rates and layering artifacts. The slow build speeds derive from the serial nature of nearly every available AM technique, typically requiring hours to make a structure. Layer artifacts arise from the discretization of a digital computer-aided design (CAD) model into 2D planes, degrading the surface characteristics of finished parts, and making some overhanging and spanning geometries impossible without support material. The volumetric approach reported here removes both of these constraints simultaneously.

To examine this more closely, AM processes can be grouped by the dimensionality of their unit operation. Point-based approaches that use a 0D voxel as their fundamental operation include methods such as laser scanning stereolithography (SLA) and its derivatives (*2*), selective laser melting (*3*), and direct laser writing (DLW) (*4*). Extrusion-based filament methods such as direct ink writing (DIW) (*5*), direct metal writing (*6*), and fused filament fabrication [more often known by the trademarked term fused deposition modeling (FDM)] (*7*) use a 1D fundamental unit. Although DLW and DIW allow some capability to build out-of-plane unsupported structures, it is highly limited and still requires serial deposition of 0D or 1D elements. In a number of recent reports, including projection micro-stereolithography (PμSL) (*8*, *9*), continuous liquid interface printing (CLIP) (*10*), and diode AM (DiAM) (*11*), complete 2D layers are formed in a single operation.

Advancing into the realm of forming complex 3D volumes as unit operations is one of the last remaining barriers to overcome for rapid 3D part fabrication spanning all three spatial dimensions. This leap continues to present conceptual and technical barriers. To date, volumetric 3D structures patterned in a single operation have not been demonstrated outside the realm of interference lithography of polymers (*12*–*14*). The resulting photonic crystals are submicrometer lattices with useful properties (*15*), but one of the part dimensions must always be orders of magnitude smaller than the others. Even when such lattices are modulated by larger-scale aperiodic features (*16*), this approach is only suitable for patterning thin photopolymer layers. Moreover, no existing technologies can produce structures without a substrate.

Here, we describe a new paradigm in photopolymer-based additive fabrication that allows the formation of complex aperiodic 3D volumes as a unit operation, with no substrate or support structures required. This is accomplished by the superposition of patterned optical fields from multiple beams projected into a photosensitive resin. The requirement for superimposing multiple patterned beams is driven by the limitations of physical optics. Scalar diffraction theory, after Abbe and Rayleigh, makes clear that for a single-beam optical system, axial resolution $d_z \approx \frac{2\lambda}{NA^2}$ is significantly worse than lateral resolution $d_{xy} \approx \frac{\lambda}{2NA}$ (NA is the numerical aperture), even for the highest NA systems (NA = 1.4 to 1.5). These same limitations have been explored, but not overcome, by investigators developing algorithms to project 3D holographic optical fields with arbitrary intensity distributions at multiple axial planes (*17*, *18*) or in a 3D volume (*19*). In all cases, axial feature spacing must be 10- to 100-fold greater than the in-plane feature spacing. The volumetric fabrication modality described here intersects orthogonally directed beams within the build volume such that, in their superimposed intensity profile, each beam compensates for the others' limited axial resolution. We demonstrate the fabrication of complex, millimeter-scale aperiodic structures and report on our initial study of key process parameters. With optimization, we expect this approach to be capable of producing features at the diffraction limit of the optical system.

A system designed for this fabrication approach must incorporate three key elements for successfully producing volumetric 3D structures. First, the optical fields must be patterned such that the required peak dose distribution accumulates simultaneously at all locations that need to be cured within the resin. Second, each beam's lateral intensity profile

[1]Lawrence Livermore National Laboratory, Livermore, CA 94550, USA. [2]Department of Electrical Engineering and Computer Science, Massachusetts Institute of Technology, Cambridge, MA 02139, USA. [3]Department of Mechanical Engineering, University of Rochester, Rochester, NY 14627, USA. [4]Department of Mechanical Engineering, University of California, Berkeley, Berkeley, CA 94720, USA. [5]Department of Electrical Engineering and Computer Science, University of California, Berkeley, Berkeley, CA 94720, USA. [6]Department of Mechanical Engineering, Massachusetts Institute of Technology, Cambridge, MA 02139, USA.
*Corresponding author. Email: shusteff1@llnl.gov (M.S.); nicfang@mit.edu (N.X.F.); spadaccini2@llnl.gov (C.M.S.)

Downloaded from http://advances.sciencemag.org/ on December 10, 2017

must be tuned to compensate for the other beams' limited axial resolution and for depth-dependent energy absorption in the resin. Third, molecular oxygen (O_2) dissolved in the resin (or another polymerization-inhibiting species mixed into the formulation) must be used to provide the nonlinearity necessary for "threshold" behavior in the polymerization process. The combination of these elements allows the desired geometry to be fully defined in 3D in a single operation. Although we implement holographic (phase-controlled) beam shaping to deliver the target patterns into the resin, the same may be accomplished by other methods (for example, amplitude modulation and image relaying) so long as the abovementioned process requirements are met.

Figure 1 presents a schematic overview of the three-beam superposition system architecture. The three orthogonal beams intersecting in the resin may be produced by independent sources; we generate them by deflecting subregions of a single holographically generated image using 45° mirrors (Fig. 1, inset). The details of the optical path and the calculation of computer-generated holograms (CGHs), which are the basis for generating the target intensity distribution $I_{HP}(x, y)$ at the hologram plane (HP in Fig. 1), are given in the Supplementary Materials. The intensity field $I_{HP}(x, y)$is image-relayed to the photopolymer resin container at a suitable magnification factor ($M = 2$ in our system). Designed for millimeter-scale part sizes, the final image relay optics in the present system have a focal length of 250 mm (NA ≈ 0.05), with a field of view of 25 mm × 25 mm, and each beam's depth of focus is approximately 10 mm. Thus, the unequal path lengths between the central beam and the folded side and bottom beams are inconsequential. Fabrication at larger or smaller structure size scales is possible by choosing a different magnification for these final optics and adding phase curvature to the hologram for the image regions deflected by mirrors. However, the minimum achievable feature size depends on the O_2 diffusion and exposure time parameters, as discussed below.

Oxygen inhibition of the free radical polymerization reaction is a critical aspect that enables this fabrication paradigm. Other inhibitor species, such as hydroquinone or 2,2-diphenyl-1-picrylhydrazyl, may be used as part of the resin formulation. However, without deliberate efforts to purge it, molecular O_2 is always present in resins open to the ambient, so in this work, we have emphasized understanding and leveraging its effects. The role of dissolved O_2 as a scavenger of free radicals in photopolymer systems has long been known and has been studied in experimental (*20*) and model systems (*21*, *22*). Because the rate constant of radical scavenging by O_2 (k_{O_2} ~ 10^7 to 10^8 liter mol^{-1} s^{-1} in similar resins) (*23*) is much greater than that for polymer chain propagation (k_p ~10^3 to 10^4 liter mol^{-1} s^{-1}), at the start of an exposure, nearly all photoinitiator (PI) radicals react with O_2 molecules until the local O_2 concentration has been depleted to an equilibrium (*23*) at which the polymerization reaction rate can compete with it. This provides a minimum volumetric energy dose threshold that limits the spatial extent of the polymerization. Our experimental results in this work are well explained by existing free-radical photopolymerization models (*20*–*23*), indicating that previously developed analytical and numerical frameworks can be successfully leveraged to further explore and develop this fabrication paradigm.

RESULTS AND DISCUSSION

Figure 1 (B to G) shows a representative variety of geometries that can be fabricated by this method, including beams, planes, and struts at arbitrary angles, lattices, and symmetric and asymmetric geometries. Significantly, no constraints exist on span, bridge, and cantilever elements, and curves may be produced without layering artifacts, which are all major challenges with standard AM layer-by-layer approaches. No supporting substrate is required during the build (although one can be used when desired). This indicates that very soft materials such as hydrogels can be fabricated wholly in situ, which, fabricated by other means, would not be self-supporting or would be damaged or destroyed by shear forces arising from fluid motion. Some structures fabricated in the present work were extremely compliant; however, full characterization of the mechanical properties of fabricated structures was outside the scope of the present study. Exploring the mechanical performance

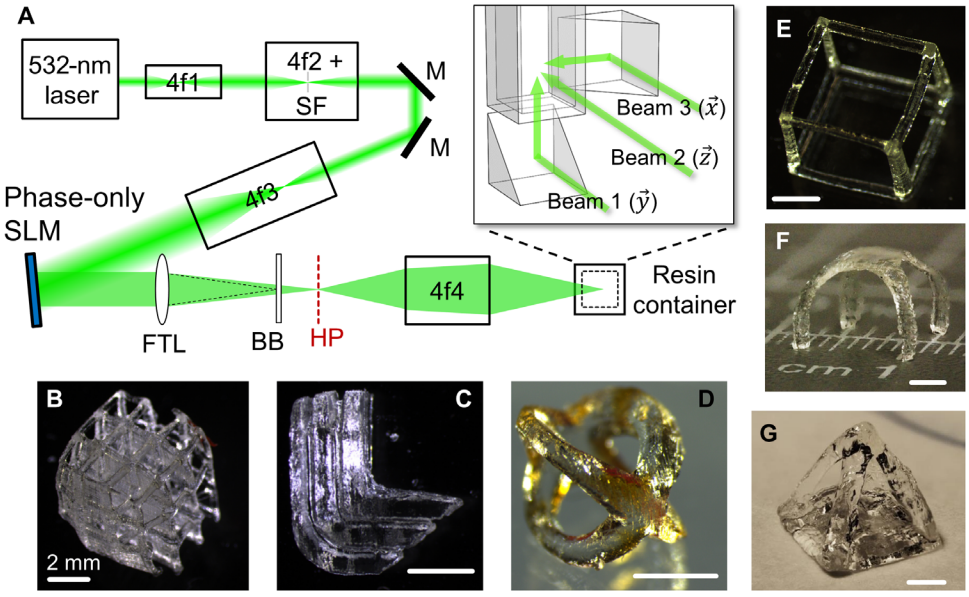

Fig. 1. Holographic volumetric 3D fabrication system schematic and example structures. (**A**) SLM, liquid crystal on silicon spatial light modulator; FTL, Fourier transform lens; BB, beam block to eliminate undiffracted light; HP, hologram plane; 4f*N*, telescope lens pairs in the "4-*f*" configuration used for beam expansion or image relaying [4f2 incorporates a pinhole spatial filter (SF)]. The inset image details the configuration of 45° prism mirrors for directing image subcomponent beams at orthogonal directions into the resin volume. (**B** to **G**) Structures fabricated using this system, each from a single exposure of 5- to 10-s duration. Scale bars, 2 mm.

Downloaded from http://advances.sciencemag.org/ on December 10, 2017

of fabricated structures, in conjunction with the degree of cure of the polymer, is an important direction for further investigation.

Our results indicate that structures can be successfully fabricated with exposures lasting 1 to 25 s and incident laser intensities between 6 and 45 mW for each beam (fig. S1). We find that the resin must typically absorb a minimum of 200 to 300 mJ/cm^3 of energy for a part to form in the presence of ambient O_2, with additional energy required under certain conditions discussed below. The smallest self-supporting features we have fabricated are approximately 300 to 400 μm in size (mainly due to the softness of the smallest struts), exhibiting surface roughness on the scale of 100 to 200 μm (primarily due to laser speckle–induced spatial noise; see the Supplementary Materials). However, these are not the fundamental capability limits for this technology, as we discuss below, because these limits will depend on optimizing the resin to balance viscosity and O_2 diffusivity. We expect this approach to be capable of fabrication at or near the diffraction limit of the optical system, which is 20 to 50 μm for the current configuration.

The results summarized in Fig. 2 reveal a number of important characteristics of this process. First, we can identify a fabrication regime in which the time for structure formation is dominated by the resin induction time t_i—sometimes also called inhibition time. This is the period required to deplete dissolved O_2 and allow polymerization to proceed. In the context of this data set, the measured gel threshold times t_{G3} and t_{G2} (defined in Materials and Methods) are approximately equal to the inhibition time in three- and two-beam regions. In general, this induction time can be estimated as

$$t_i = \frac{[O_{2,0}]}{R_{init}} \quad (1)$$

where $[O_{2,0}]$ is the initial dissolved O_2 concentration, and

$$R_{init} = \frac{\varphi I_{abs}(x, y, z)}{N_A h\nu} \quad (2)$$

is the photoradical generation rate, in which φ is the quantum efficiency and $I_{abs}(x, y, z)$ is the (3D spatially varying) absorbed light intensity per unit volume, which the denominator converts from milliwatts per cubic centimeter into molar terms, using Avogadro's constant N_A and the

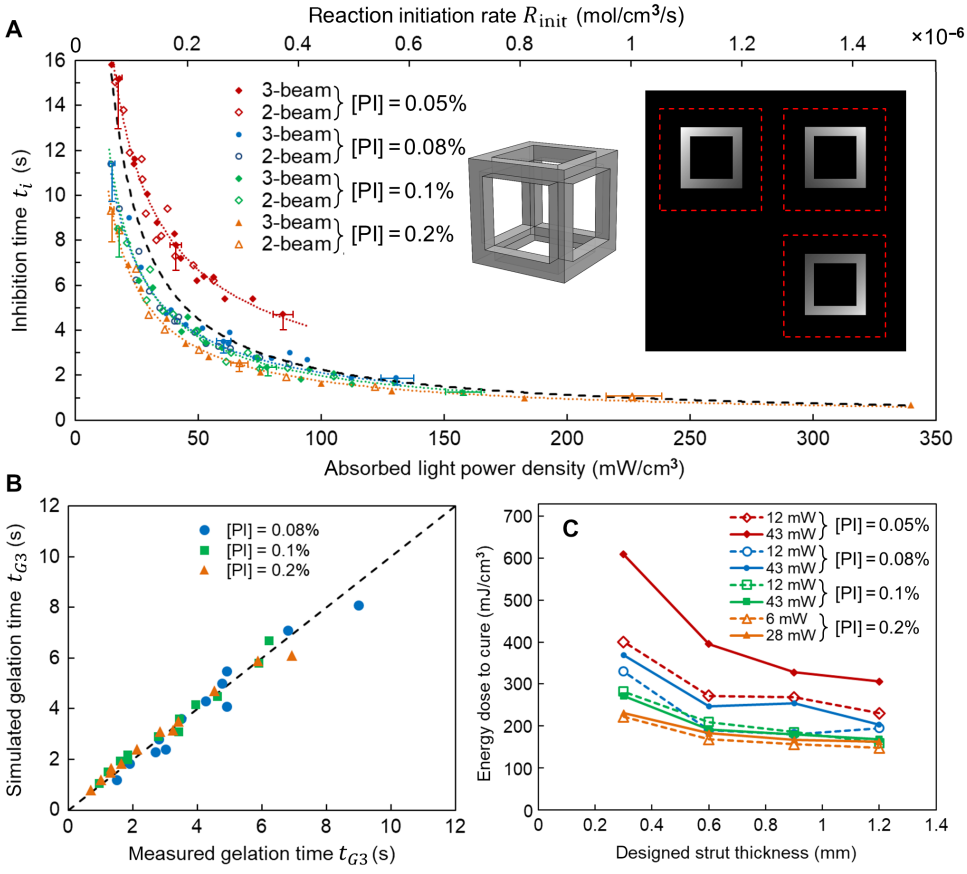

Fig. 2. Induction time and curing dose dependence on key process parameters. (**A**) Summary of polymerization induction times t_i before gelation in three-beam regions, as determined by the first appearance of cube edges, showing strut sizes from 0.6 to 1.2 mm. Error bars are estimates of data reproducibility based on $N = 3$ measurements at typical conditions, given one-sided due to the tendency of cure time measurements to bias upward from gradual resin degradation. Colored dotted lines are power-law fits to the data at each PI concentration. The black dashed line is the equation $t_i = \frac{[O_{2,0}]}{R_{init}}$, where the variables on the right-hand side are estimated from measurements of system parameters or similar resin formulations. The insets show a typical cube structure used to generate these data, and an intensity-compensated image that was used for exposure. (**B**) Comparison of model-predicted and experimentally measured three-beam gel times t_{G3}, with the dashed line indicating unit slope. Data from three different laser powers between 6 and 40 mW are represented at each PI concentration. (**C**) Energy doses required to cure cube struts (three-beam regions), plotted for the highest and lowest beam power used at each PI concentration.

Downloaded from http://advances.sciencemag.org/ on December 10, 2017

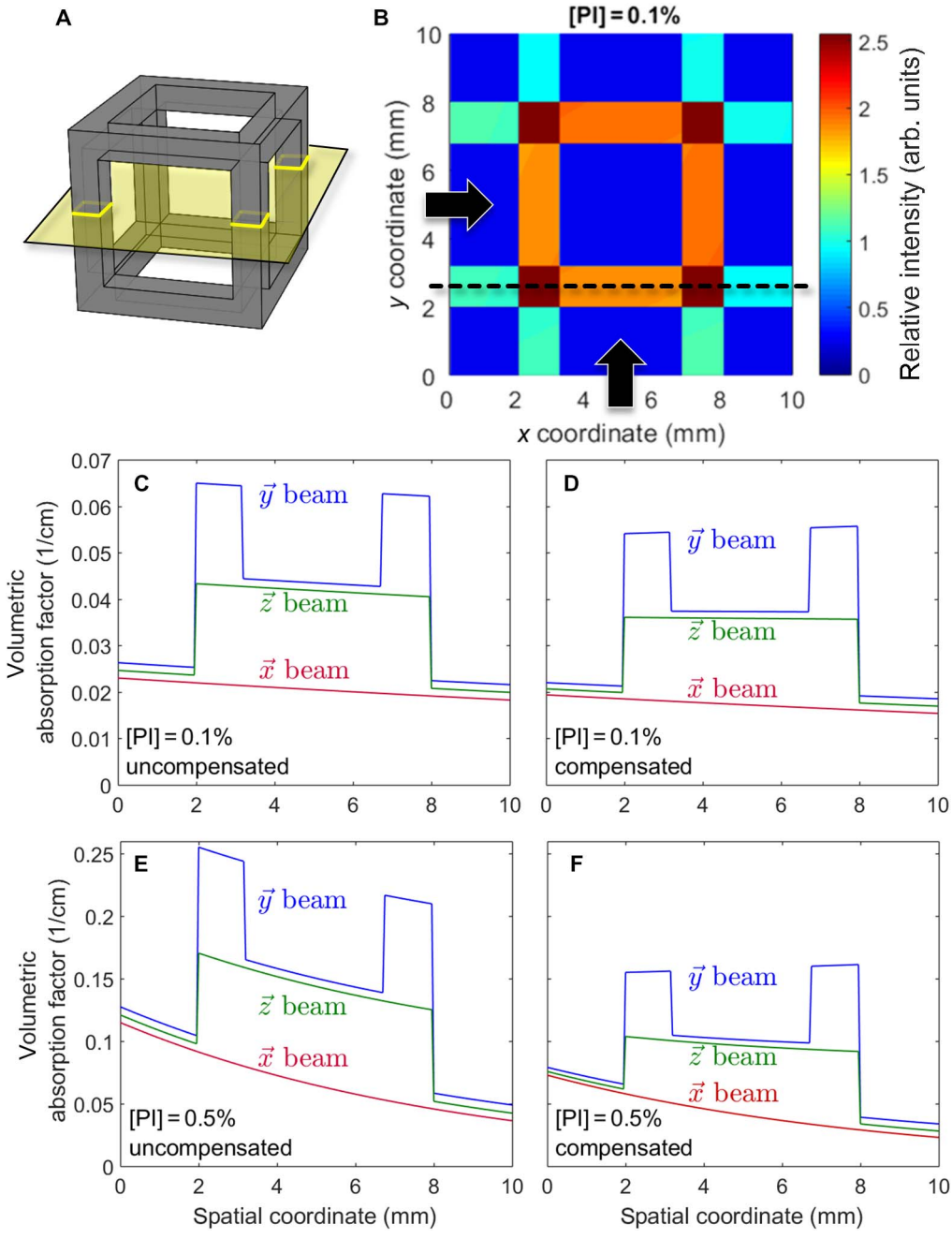

Fig. 3. Optical attenuation and three-beam superposition compensation model. (**A**) Representative plane at which all three-beam contributions are calculated, shown in (**B**) as a heat map representing relative intensities. Beams 1 and 2 are incident from the left and bottom as indicated by black arrows, and beam 3 is directed into the page. (**C** and **E**) Summed volumetric absorption values from three-beam superposition, without compensation, at the location marked by the dashed line in (B), comparing different [PI]. (**D** and **F**) Intensity profiles at the same [PI] but compensated to attain equal peak intensity in three-beam overlap regions.

energy per photon $h\nu$. A more detailed derivation of I_{abs} and its spatial dependence is given in the Supplementary Materials.

The inverse relationship of Eq. 1 between t_i and R_{init} holds under two conditions. First, when the initial concentration of PI [PI_0] is in excess relative to [$O_{2,0}$], R_{init} remains approximately constant throughout the induction period; this is indicated by the curves in Fig. 2A for 0.08, 0.10, and 0.20% [PI_0], which largely overlap within experimental error. When [PI_0] is approximately equal to [$O_{2,0}$] (in absolute molar terms), by the time that dissolved O_2 has been depleted, little to no initiator remains available for polymerization to proceed, and induction times are significantly extended. We see this in Fig. 2A for the resin with 0.05% [PI_0] (which is $\approx 1.6 \times 10^{-3}$ M), approximately matching [$O_{2,0}$] $\approx 1.2 \times 10^{-3}$ M (*24*), where the t_i values are extended relative to the simple model of Eq. 1 (see the Supplementary Materials for additional discussion). Below this threshold, curing times are extended many-fold, or even indefinitely, such that complete structures do not form even when light energy continues being delivered to the resin. This behavior indicates that resins should be formulated with [PI_0] > [$O_{2,0}$] for robust process control.

Downloaded from http://advances.sciencemag.org/ on December 10, 2017

The second condition for the relationship of Eq. 1 to remain valid reveals a feature size dependence because of the rediffusion of O_2 into curing regions. When the strut thickness length scale is comparable to the O_2 diffusion length over the exposure time scale, additional O_2 diffusing in during exposure requires additional energy for the part to cure. For the low-viscosity PEGDA resin used here ($\mu \approx 12$ centipoise), O_2 diffusivity is estimated to be $D_{O_2} \approx 1.5 \times 10^{-9}$ m^2/s based on diffusivity in similar resins (*20*–*22*), which corresponds to a diffusion time $\tau_{O_2} = \frac{x^2}{6D_{O_2}}$ of 2 to 3 s over length scale $x \approx 100$ to 200 μm (from strut edge to center). For this reason, in Fig. 2C, we observe an increase in required curing energies for struts thinner than approximately 0.4 mm and virtually no size dependence above this size (the results for 0.3 mm struts are omitted from Fig. 2A, so no size dependence is seen). This trend is reflected in the computational model as well. From these computational simulation results, validated against experimental data (Fig. 2B), we expect that successfully forming structures with features down to the ~10- to 100-μm size range is possible. We anticipate that fabrication of these finely detailed structures will require running at reduced O_2 concentration, with a similar degree of control as in other microscale SLA methods (*25*), or running with O_2 completely depleted and another inhibitor in the resin.

The requirement that all cured areas simultaneously attain the same absorbed energy dose requires compensation of each beam's depth-dependent energy absorption in the resin by applying transverse intensity gradients to the other beams (thus, all beams are intensity-modulated, each compensating for the other two). This is carried out using a 3D light attenuation and absorption model governed by the Beer-Lambert law, and an example of an intensity-compensated image can be seen in the right inset of Fig. 2A. Figure 3 summarizes the use of this compensation scheme, from which the resulting gradients are applied to the target intensity distribution before CGH computation. The model implies an effective upper bound on resin absorbance (here approximately 0.5% [PI_0]). Absorption is a nonlinear phenomenon, and beyond a certain point, the spatial nonuniformity of absorbed energy cannot be adequately compensated by the linear superposition of intensity profiles (see the Supplementary Materials and fig. S2, C to F).

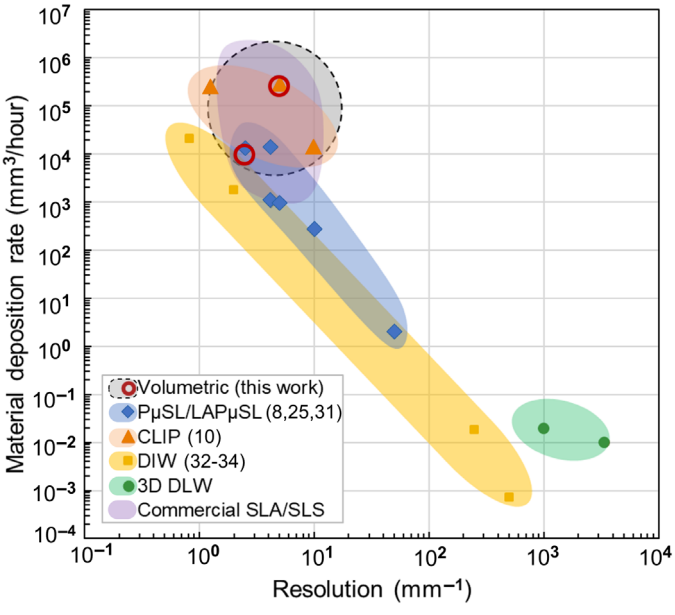

Fig. 4. A process performance comparison of volumetric fabrication to other polymer-based AM methods. Resolution is defined as 1/(2δ), where δ is the minimum feature size. The gray dashed boundary oval encloses fabrication results from two scenarios and represents the authors' speculation regarding the near-term potential of the volumetric fabrication method reported in this work. Plotted data points represent specific published results or system operating parameters known first hand to the authors. PμSL/LAPμSL, projection micro-stereolithography and its large-area variant (*8*, *25*, *31*); CLIP (*10*), continuous liquid interface printing; DIW, direct ink writing (*32*–*34*); DLW, direct laser writing; SLA, stereolithography; SLS, selective laser sintering. Commercial system performance is based on the manufacturer's specifications.

Knowing the upper and lower bounds on [PI], the interaction with the other process parameters can be more elucidated. The product of [PI] and light intensity, *I*, determines the time scale for part formation, and this time scale must be shorter than τ_{O_2}, the O_2 diffusion time scale for feature sizes of interest. The upper limit on [PI] therefore sets an effective minimum light power requirement for the process. The O_2 diffusion time scale, τ_{O_2}, can be adjusted by formulating a higher-viscosity resin to slow O_2 diffusion, which can also mitigate any buoyant settling (the cured polymer is denser than the liquid monomer) or thermally induced convection. From these results, it becomes clear that future investigation should be aimed toward investigating resins with higher viscosity, reduced O_2 solubility (or O_2 controlled by purging with inert gas), and alternative inhibitors. In combination with reducing the spatial noise from the optical system (here incurred due to holographic reconstruction using coherent light), our modeled and measured results indicate that diffraction-limited fabrication performance is attainable.

This novel approach to 3D fabrication lends itself to implementation in a variety of ways. Knowing the bounds of the key process parameters discovered in this work, other AM systems may be designed based on this volumetric paradigm. In general, the throughput of these systems is limited only by the size of the resin container and the available optical power. For instance, reconfigured around a larger resin bath, the maximum 6-W output of the 532-nm source used here can be readily redistributed over a 10× larger area for each beam, corresponding to a 100× greater build rate. Fabrication can also be accomplished by amplitude-controlling spatial light modulators (such as digital micromirror arrays) illuminated by incoherent sources such as light-emitting diodes, which do not suffer from speckle and therefore have lower inherent spatial noise. This is likely to reduce the system's overall optical complexity and cost, with little loss of performance. A comparison of the resolution and build speed of the present system to existing polymer-based methods is presented in Fig. 4, showing that this approach is, at a minimum, competitive with the highest-throughput commercial AM systems and has the potential to break through the present trade-off between build speed and resolution.

In its present implementation, the main limitation on geometries that can be fabricated by this approach arises from the prismatic ("extruded shape") nature of the overlapping beams. This can be readily circumvented by building up a more complex geometry from time-sequenced exposures of simpler subgeometries. Suitable adjustments must be made to the illumination pattern from exposure to exposure, and the resin viscosity may need to be tuned as well.

As a 3D polymer–based fabrication technique, this method is notable for relying on a single-photon absorption process to drive polymerization while achieving equally high spatial resolution in all three dimensions. The only technique capable of similar bulk-volume fabrication away from surfaces is DLW, which relies on two-photon polymerization and therefore requires expensive femtosecond lasers to attain beam intensities of terawatts per square centimeter needed for simultaneous absorption of multiple photons (*26*). The work reported here, in

Downloaded from http://advances.sciencemag.org/ on December 10, 2017

contrast, allows the use of relatively inexpensive low-power sources. Here, similarly to two-photon DLW, spatial confinement is a consequence of a threshold behavior that arises due to the nonlinearity of polymerization in the presence of an inhibitor (O_2). Although two-photon DLW exploits this nonlinearity via its nonlinear (square) dependence of absorption on the incident light intensity, our method relies on multibeam superposition, a simpler principle to implement. We therefore expect this new fabrication framework to open a major new direction of research in rapid 3D structure fabrication owing to its low cost, flexibility, speed, and geometric versatility.

MATERIALS AND METHODS

Exposures in this system were carried out in a resin volume of 1.5 ml contained in a photometer cuvette with an internal cross section of 10 mm × 10 mm (3-G-10, Starna Cells), with 1.25-mm-thick optical-quality sides and bottom, providing optical access from all directions. The resin consisted of low–molecular weight poly(ethylene glycol) diacrylate (PEGDA; M_n = 250; Sigma-Aldrich), with 0.05 to 0.2% (w/w) Irgacure 784 initiator (BASF) sensitive at the 532-nm wavelength of the laser source. An ideal resin for multibeam superposition should have uniform absorbance throughout the build volume (fig. S2). In a real resin, this condition can be approached by minimizing the PI concentration so long as total absorbed energy is sufficient to attain curing thresholds with the available light power. The energy absorbed can be estimated for any source-resin combination by directly measuring the absorbance at the relevant wavelength and setting the delivered energy dose, as described in the Supplementary Materials.

To carry out a study of the major parameters affecting curing kinetics, a family of cube structures (Fig. 2A, left inset) 6 mm on a side was used as test objects, with strut sizes ranging from 0.3 to 1.2 mm. The cube structure, although simple, provided a generic geometry for calculating the necessary lateral compensation in the intersecting beam profiles and for assessing the spatial uniformity of the target energy dose based on the relative timing of cube edge appearance. We carried out experiments for PI concentrations between 0.05 and 0.2% by weight at a range of laser power settings. This geometry allowed measurement of key time points during the polymerization process, as structural features began to appear in the resin bulk. The first solidification of cube edges was assumed to roughly correspond to the polymer gel point of approximately 30% double-bond conversion, according to the classic descriptions of gelation by Flory (*27*) and Stockmayer (*28*). These are the highest-intensity regions with contributions from all three superposed beams (referred to as the three-beam curing threshold t_{G3}). Continuing the exposure beyond this point led to the appearance of cube faces, as regions illuminated by only two beams absorbed sufficient energy across the gel threshold at t_{G2}. Eventually, single-beam illuminated regions also solidified (see fig. S3). The time between t_{G3} and t_{G2} provides the useful process window for optimizing the 3D structure. For the structures produced in this work, the optimal cure time t_{opt} (data in fig. S1) was defined as the time just before the two-beam threshold.

We measured the values of t_{G3} and t_{G2} at different light intensities and resin compositions by making exposures of varying duration controlled by an electronic shutter (Uniblitz, Vincent Associates). After each timed exposure, the part formed in the cuvette was easily evaluated by visual inspection to determine its state relative to the threshold time points described above. The first appearance of cube edge struts corresponded to t_{G3}, and the first appearance of cube faces corresponded to t_{G2}. Post-illumination polymerization outside gelled regions was assumed to be negligible relative to the size scales of our features due to O_2 inhibition (*29*). After exposure, parts were removed from the container by first aspirating excess unpolymerized liquid resin by pipette and then rinsing the part for 30 s in ethanol. Structural features were measured using a calibrated stereomicroscope (Zeiss).

To further study our process conditions and gain additional predictive power, we used a commercial finite element package (COMSOL Multiphysics) to implement a comprehensive reaction-diffusion model of the photopolymerization process, after the framework described by Bowman and coworkers (*21*, *22*, *30*). The model details are given in the Supplementary Materials, and comparison with experimental results is made in Fig. 2.

SUPPLEMENTARY MATERIALS

Supplementary material for this article is available at http://advances.sciencemag.org/cgi/content/full/3/12/eaao5496/DC1

Supplementary Materials and Methods

fig. S1. Experimentally measured cure times for the full range of illumination intensities.

fig. S2. Details of intensity attenuation effects and compensation for resins with differing absorption coefficients.

fig. S3. Progression of multibeam 3D volumetric polymerization of cube structures and eventual overcuring.

fig. S4. Representative results from the polymerization simulations.

fig. S5. Effects of curing conditions on feature resolution and distortion.

References (*35*–*42*)

REFERENCES AND NOTES

1. E. MacDonald, R. Wicker, Multiprocess 3D printing for increasing component functionality. *Science* **353**, aaf2093 (2016).
2. F. P. W. Melchels, J. Feijen, D. W. Grijpma, A review on stereolithography and its applications in biomedical engineering. *Biomaterials* **31**, 6121–6130 (2010).
3. C. Y. Yap, C. K. Chua, Z. L. Dong, Z. H. Liu, D. Q. Zhang, L. E. Loh, S. L. Sing, Review of selective laser melting: Materials and applications. *Appl. Phys. Rev.* **2**, 041101 (2015).
4. T. Gissibl, S. Thiele, A. Herkommer, H. Giessen, Two-photon direct laser writing of ultracompact multi-lens objectives. *Nat. Photonics* **10**, 554–560 (2016).
5. J. A. Lewis, Direct ink writing of 3D functional materials. *Adv. Funct. Mater.* **16**, 2193–2204 (2006).
6. W. Chen, L. Thornley, H. G. Coe, S. J. Tonneslan, J. J. Vericella, C. Zhu, E. B. Duoss, R. M. Hunt, M. J. Wight, D. Apelian, A. J. Pascall, J. D. Kuntz, C. M. Spadaccini, Direct metal writing: Controlling the rheology through microstructure. *Appl. Phys. Lett.* **110**, 094104 (2017).
7. A. J. L. Morgan, L. Hidalgo San Jose, W. D. Jamieson, J. M. Wymant, B. Song, P. Stephens, D. A. Barrow, O. K. Castell, Simple and versatile 3D printed microfluidics using fused filament fabrication. *PLOS ONE* **11**, e0152023 (2016).
8. X. Zheng, H. Lee, T. H. Weisgraber, M. Shusteff, J. DeOtte, E. B. Duoss, J. D. Kuntz, M. M. Biener, Q. Ge, J. A. Jackson, S. O. Kucheyev, N. X. Fang, C. M. Spadaccini, Ultralight, ultrastiff mechanical metamaterials. *Science* **344**, 1373–1377 (2014).
9. M. P. Lee, G. J. T. Cooper, T. Hinkley, G. M. Gibson, M. J. Padgett, L. Cronin, Development of a 3D printer using scanning projection stereolithography. *Sci. Rep.* **5**, 9875 (2015).
10. J. R. Tumbleston, D. Shirvanyants, N. Ermoshkin, R. Janusziewicz, A. R. Johnson, D. Kelly, K. Chen, R. Pinschmidt, J. P. Rolland, A. Ermoshkin, E. T. Samulski, J. M. DeSimone, Continuous liquid interface production of 3D objects. *Science* **347**, 1349–1352 (2015).
11. M. J. Matthews, G. Guss, D. R. Drachenberg, J. A. Demuth, J. E. Heebner, E. B. Duoss, J. D. Kuntz, C. M. Spadaccini, Diode-based additive manufacturing of metals using an optically-addressable light valve. *Opt. Express* **25**, 11788–11800 (2017).
12. Y. Lin, A. Harb, K. Lozano, D. Xu, K. P. Chen, Five beam holographic lithography for simultaneous fabrication of three dimensional photonic crystal templates and line defects using phase tunable diffractive optical element. *Opt. Express* **17**, 16625–16631 (2009).
13. K. Ohlinger, J. Lutkenhaus, B. Arigong, H. Zhang, Y. Lin, Spatially addressable design of gradient index structures through spatial light modulator based holographic lithography. *J. Appl. Phys.* **114**, 213102 (2013).
14. H. Ning, J. H. Pikul, R. Zhang, X. Li, S. Xu, J. Wang, J. A. Rogers, W. P. King, P. V. Braun, Holographic patterning of high-performance on-chip 3D lithium-ion microbatteries. *Proc. Natl. Acad. Sci. U.S.A.* **112**, 6573–6578 (2015).

Downloaded from http://advances.sciencemag.org/ on December 10, 2017

15. M. C. R. Leibovici, T. K. Gaylord, Photonic-crystal waveguide structure by pattern-integrated interference lithography. *Opt. Lett.* **40**, 2806–2809 (2015).
16. M. C. R. Leibovici, T. K. Gaylord, Custom-modified three-dimensional periodic microstructures by pattern-integrated interference lithography. *J. Opt. Soc. Am. A* **31**, 1515–1519 (2014).
17. J. Xia, H. Yin, Three-dimensional light modulation using phase-only spatial light modulator. *Opt. Eng.* **48**, 020502 (2009).
18. P. Wang, R. Menon, Optical microlithography on oblique and multiplane surfaces using diffractive phase masks. *J. Micro/Nanolith. MEMS MOEMS* **14**, 023507 (2015).
19. G. Whyte, J. Courtial, Experimental demonstration of holographic three-dimensional light shaping using a Gerchberg–Saxton algorithm. *New J. Phys.* **7**, 117 (2005).
20. D. Dendukuri, P. Panda, R. Haghgooie, J. M. Kim, T. A. Hatton, P. S. Doyle, Modeling of oxygen-inhibited free radical photopolymerization in a PDMS microfluidic device. *Macromolecules* **41**, 8547–8556 (2008).
21. M. D. Goodner, C. N. Bowman, Development of a comprehensive free radical photopolymerization model incorporating heat and mass transfer effects in thick films. *Chem. Eng. Sci.* **57**, 887–900 (2002).
22. A. K. O'Brien, C. N. Bowman, Impact of oxygen on photopolymerization kinetics and polymer structure. *Macromolecules* **39**, 2501–2506 (2006).
23. C. Decker, A. D. Jenkins, Kinetic approach of oxygen inhibition in ultraviolet- and laser-induced polymerizations. *Macromolecules* **18**, 1241–1244 (1985).
24. S. C. Ligon, B. Husár, H. Wutzel, R. Holman, R. Liska, Strategies to reduce oxygen inhibition in photoinduced polymerization. *Chem. Rev.* **114**, 557–589 (2014).
25. X. Zheng, J. Deotte, M. P. Alonso, G. R. Farquar, T. H. Weisgraber, S. Gemberling, H. Lee, N. Fang, C. M. Spadaccini, Design and optimization of a light-emitting diode projection micro-stereolithography three-dimensional manufacturing system. *Rev. Sci. Instrum.* **83**, 125001 (2012).
26. S. Wu, J. Serbin, M. Gu, Two-photon polymerisation for three-dimensional micro-fabrication. *J. Photochem. Photobiol. A Chem.* **181**, 1–11 (2006).
27. P. J. Flory, Molecular size distribution in three dimensional polymers. I. Gelation. *J. Am. Chem. Soc.* **63**, 3083–3090 (1941).
28. W. H. Stockmayer, Theory of molecular size distribution and gel formation in branched-chain polymers. *J. Chem. Phys.* **11**, 45–55 (1943).
29. J. B. Mueller, J. Fischer, F. Mayer, M. Kadic, M. Wegener, Polymerization kinetics in three-dimensional direct laser writing. *Adv. Mater.* **26**, 6566–6571 (2014).
30. K. S. Anseth, C. M. Wang, C. N. Bowman, Reaction behaviour and kinetic constants for photopolymerizations of multi(meth)acrylate monomers. *Polymer* **35**, 3243–3250 (1994).
31. X. Zheng, W. Smith, J. Jackson, B. Moran, H. Cui, D. Chen, J. Ye, N. Fang, N. Rodriguez, T. Weisgraber, C. M. Spadaccini, Multiscale metallic metamaterials. *Nat. Mater.* **15**, 1100–1106 (2016).
32. G. M. Gratson, F. García-Santamaría, V. Lousse, M. Xu, S. Fan, J. A. Lewis, P. V. Braun, Direct-write assembly of three-dimensional photonic crystals: Conversion of polymer scaffolds to silicon hollow-woodpile structures. *Adv. Mater.* **18**, 461–465 (2006).
33. E. B. Duoss, M. Twardowski, J. A. Lewis, Sol-gel inks for direct-write assembly of functional oxides. *Adv. Mater.* **19**, 3485–3489 (2007).
34. E. B. Duoss, T. H. Weisgraber, K. Hearon, C. Zhu, W. Small IV, T. R. Metz, J. J. Vericella, H. D. Barth, J. D. Kuntz, R. S. Maxwell, C. M. Spadaccini, T. S. Wilson, Three-dimensional printing of elastomeric, cellular architectures with negative stiffness. *Adv. Funct. Mater.* **24**, 4905–4913 (2014).
35. R. W. Bowman, M. J. Padgett, Optical trapping and binding. *Rep. Prog. Phys.* **76**, 026401 (2013).
36. M. Polin, K. Ladavac, S.-H. Lee, Y. Roichman, D. G. Grier, Optimized holographic optical traps. *Opt. Express* **13**, 5831–5845 (2005).
37. A. Georgiou, J. Christmas, J. Moore, A. Jeziorska-Chapman, A. Davey, N. Collings, W. A. Crossland, Liquid crystal over silicon device characteristics for holographic projection of high-definition television images. *Appl. Opt.* **47**, 4793–4803 (2008).
38. J.-S. Chen, D. P. Chu, Improved layer-based method for rapid hologram generation and real-time interactive holographic display applications. *Opt. Express* **23**, 18143–18155 (2015).
39. L. Golan, I. Reutsky, N. Farah, S. Shoham, Design and characteristics of holographic neural photo-stimulation systems. *J. Neural Eng.* **6**, 066004 (2009).
40. N. J. Jenness, R. T. Hill, A. Hucknall, A. Chilkoti, R. L. Clark, A versatile diffractive maskless lithography for single-shot and serial microfabrication. *Opt. Express* **18**, 11754–11762 (2010).
41. R. W. Gerchberg, W. O. Saxton, A practical algorithm for the determination of phase from image and diffraction plane pictures. *Optik* **35**, 237–246 (1972).
42. T. Haist, W. Osten, Holography using pixelated spatial light modulators—Part 1: Theory and basic considerations. *J. Micro/Nanolith. MEMS MOEMS* **14**, 041310 (2015).

Acknowledgments: We thank S. Saha and J. Oakdale for their insights and helpful discussions. **Funding:** N.X.F. acknowledges funding from the Office of Naval Research (contract N00014-13-1-0631). This work was performed under the auspices of the U.S. Department of Energy by Lawrence Livermore National Laboratory under contract DE-AC52-07NA27344 with support from Laboratory Directed Research and Development funding 14-SI-004 and 17-ERD-116 (LLNL-JRNL-732526). **Author contributions:** M.S., C.M.S., and N.X.F. designed the research; M.S., A.E.M.B., J.H., and B.E.K. carried out experiments; T.H.W. performed computational simulations; M.S., T.H.W., and R.M.P. analyzed the data; M.S. and T.H.W. wrote the manuscript; all authors reviewed and revised the manuscript. **Competing interests:** M.S., R.M.P., J.H., B.E.K., A.E.M.B., N.X.F., and C.M.S. are inventors on a nonprovisional U.S. patent application related to this work (application no. 15/651,861; filed 17 July 2017). The authors declare no other competing interests. **Data and materials availability:** All data needed to evaluate the conclusions in the paper are present in the paper and/or the Supplementary Materials. Additional data related to this paper may be requested from the authors.

Submitted 1 August 2017
Accepted 3 November 2017
Published 8 December 2017
10.1126/sciadv.aao5496

Citation: M. Shusteff, A. E. M. Browar, B. E. Kelly, J. Henriksson, T. H. Weisgraber, R. M. Panas, N. X. Fang, C. M. Spadaccini, One-step volumetric additive manufacturing of complex polymer structures. *Sci. Adv.* **3**, eaao5496 (2017).

Downloaded from http://advances.sciencemag.org/ on December 10, 2017

Science Advances

One-step volumetric additive manufacturing of complex polymer structures

Maxim Shusteff, Allison E. M. Browar, Brett E. Kelly, Johannes Henriksson, Todd H. Weisgraber, Robert M. Panas, Nicholas X. Fang and Christopher M. Spadaccini

Sci Adv **3** (12), eaao5496.
DOI: 10.1126/sciadv.aao5496

ARTICLE TOOLS http://advances.sciencemag.org/content/3/12/eaao5496

SUPPLEMENTARY MATERIALS http://advances.sciencemag.org/content/suppl/2017/12/04/3.12.eaao5496.DC1

REFERENCES This article cites 42 articles, 4 of which you can access for free
http://advances.sciencemag.org/content/3/12/eaao5496#BIBL

PERMISSIONS http://www.sciencemag.org/help/reprints-and-permissions

Use of this article is subject to the Terms of Service

Science Advances (ISSN 2375-2548) is published by the American Association for the Advancement of Science, 1200 New York Avenue NW, Washington, DC 20005. 2017 © The Authors, some rights reserved; exclusive licensee American Association for the Advancement of Science. No claim to original U.S. Government Works. The title *Science Advances* is a registered trademark of AAAS.

Downloaded from http://advances.sciencemag.org/ on December 10, 2017